North Atlantic tropical cyclone size and storm surge reconstructions from 1950-present

Avantika Gori[a], Ning Lin[a], Benjamin Schenkel[b,c], Daniel Chavas[d]

[a] *Department of Civil and Environmental Engineering, Princeton University, Princeton, NJ*

[b] *The Cooperative Institute for Severe and High-Impact Weather Research and Operations, University of Oklahoma, Norman, OK*

[c] *NOAA/OAR National Severe Storms Laboratory, Norman, OK*

[d] *Department of Earth, Atmospheric, and Planetary Sciences, Purdue University, West Lafayette, IN*

Corresponding Author: Avantika Gori, agori@princeton.edu

Key Points

- We leverage ERA5 reanalysis data combined with a physics-based wind model to estimate tropical cyclone (TC) storm size
- We develop a dataset of North Atlantic TC storm sizes (i.e. radius to maximum wind and outer size) from 1950-2020
- Using reconstructed TC sizes and a hydrodynamic model, we develop a dataset of historical storm tides from 1950-2020

Abstract

Tropical cyclones (TCs) are one of the greatest threats to coastal communities along the US Atlantic and Gulf coasts due to their extreme winds, rainfall and storm surge. Analyzing historical TC climatology and modeling TC hazards can provide valuable insight to planners and decision makers. However, detailed TC size information is typically only available from 1988 onward, preventing accurate wind, rainfall, and storm surge modeling for TCs occurring earlier in the historical record. To overcome temporally limited TC size data, we develop a database of size estimates that are based on reanalysis data and a physics-based model. Specifically, we utilize ERA5 reanalysis data to estimate the TC outer size, and a physics-based TC wind model to estimate the radius of maximum wind. We evaluate our TC size estimates using two high-resolution wind datasets as well as Best Track information for a wide variety of TCs. Using the estimated size information plus the TC track and intensity, we reconstruct historical storm tides from 1950-2020 using a basin-scale hydrodynamic model and show that our reconstructions agree well with observed peak water levels. Finally, we demonstrate that incorporating an expanded set of historical modeled storm tides beginning in 1950 can enhance our understanding of US coastal hazard. Our newly developed database of TC sizes and associated storm tides can aid in understanding North Atlantic TC climatology and modeling TC wind, storm surge, and rainfall hazard along the US Atlantic and Gulf coasts.

1. Introduction

Tropical cyclones (TCs) are one of the largest threats to coastal communities worldwide (Dullaart et al., 2021), and are the costliest natural hazard impacting the United States (Smith and Katz, 2013). Landfalling TCs can bring extreme winds, storm surges, and rainfall to coastal regions, resulting in widespread damages and loss of life. For example, the Galveston hurricane of 1900 caused at least 6,000 fatalities, and remains the deadliest US hurricane to date (Cline, 1900). More recently, Hurricanes Katrina (2005), Sandy (2012), and Harvey (2017) caused extreme flooding due to their rainfall and storm surges with total damages ranging from $80-$150 billion (2022 USD) for each of the storms (Blake et al., 2013; Blake and Zelinsky, 2017; Knabb et al., 2005). Given

the magnitude and frequency of TC-induced catastrophes, it is vital to understand and characterize the wind, rain and surge hazards from historical hurricanes. Developing spatially and temporally continuous records of TC storm characteristics and associated hazards can aid in risk assessment, emergency planning, and mitigation efforts.

TC wind, rainfall and surge severity in coastal regions depends on storm characteristics including intensity (maximum sustained wind speed – V_{max} and minimum central pressure – P_{min}), inner size (i.e. radius to maximum wind – R_{max}), translation speed, and approach angle to the coast (Irish et al., 2008; Ramos-Valle et al., 2020; Thomas et al., 2019). Peak storm surges also vary based on geographic characteristics, such as coastline shape and near-shore bathymetry (Woodruff et al., 2013), while rainfall rates are sensitive to land topography and land cover characteristics (Zhang et al., 2018). Aside from features of the synoptic-scale environment (such as vertical wind shear), V_{max} and R_{max} are often the two most important storm characteristics controlling the TC wind field (Chavas et al., 2015), peak rainfall rate (Liu et al., 2019), and peak storm surge (Bass et al., 2017).

Databases of North Atlantic TC tracks and intensities, such as the International Best Track Archive for Climate Stewardship (IBTrACS; Knapp et al., 2010), date back to the 1800's. However, detailed TC size estimates are typically only available from 1988 onward (Demuth et al., 2006). There are also numerous databases containing information about observed TC storm surges and rainfall. For example, several databases of observed storm tides from tidal gauges (https://tidesandcurrents.noaa.gov) and high-water marks (https://stn.wim.usgs.gov/FEV) are available, and these observations can provide valuable hazard information. However, their spatial coverage is limited based on the locations of tidal gauges and collected high water marks. For example, along the US coastline there are only 100 tidal gauges with more than 30 years of data. The relatively sparse distribution of tidal gauges may not capture peak water levels induced by TCs (Haigh et al., 2014; Pugh, 1987), and these gauges may fail during high intensity events (Beven et al., 2008; Fritz et al., 2007). Other storm surge databases drawing from observations, technical reports, journal articles, and newspapers (Needham et al., 2015; Needham and Keim, 2012) have estimated the location and magnitude of peak storm surges for many historical TCs, although they do not provide spatially continuous storm

surge estimates for each event. As with storm surge observations, peak wind speed and rainfall observations are available at gauge locations (Menne et al., 2012) dating back to the late 1800's. However, spatially continuous, sub-daily wind field or rainfall observations, such as data derived from satellite and radar, is only available starting in the late 1990's (Chavas and Vigh, 2014; Huffman et al., 2021; Lin and Mitchell, 2005; Powell et al., 1998). Moreover, since satellite data is often only available at irregular sampling intervals, snapshots of wind and rainfall estimates from satellite products may not be temporally continuous. Given the dearth of observations, we can instead use physics-based wind models, rainfall models, and high-resolution hydrodynamic models to reconstruct spatially and temporally continuous estimates of historical TC hazards and structure. Currently, model-based datasets of historical TC storm tides and winds only date back to 1988 (Done et al., 2020; Marsooli and Lin, 2018; Muis et al., 2019) due to temporally limited TC size data. Expanding these datasets to incorporate hazard estimates from earlier TCs would greatly enhance our understanding of historical TC risk.

To overcome temporally limited TC size data, reanalysis datasets, which are based on operational numerical weather prediction models and data assimilation, and physics-based TC models may be used together to estimate wind field structure. Typical global reanalysis products, with horizontal grid resolution ranging from 0.25°-0.7°, are often unable to resolve the TC inner core (Hodges et al., 2017; Schenkel and Hart, 2012). However, these datasets may be able to accurately represent features of the outer TC wind field (Schenkel et al., 2017), where there is minimal convection and the lower troposphere is approximately in radiative-subsidence balance (Chavas et al., 2015). The size of the outer TC wind field is often defined as the radius of the outermost closed isobar (Merrill, 1984), or radius of a specified mean azimuthal weak wind speed (e.g., radius of 2 – 12 m/s azimuthal winds; Chavas et al., 2016; Chavas and Vigh, 2014; Schenkel et al., 2018, 2017). Previous studies have found that reanalysis datasets can reasonably represent TC outer size metrics, such as radii of azimuthal-mean 6-8 m/s azimuthal winds (Bian et al., 2021; Schenkel et al., 2017). Using reanalysis-based estimates of TC outer size and V_{max} based on Best Track data, parametric TC wind models may be used to characterize the full TC wind field. Specifically, the physics-based complete TC wind model of Chavas et al. (2015; hereafter CLE15) can realistically

reproduce the entire TC wind field structure including hard to measure quantities like R_{max} based on outer size and V_{max} (Chavas et al., 2015; Lin and Chavas, 2012). Recently, Chavas and Knaff (2022) demonstrated how the CLE15 theory is quite similar to observations in their effort to create a simple physics-based empirical model to estimate R_{max} from the radius of 17.5 m/s wind that compares well against R_{max} observations from historical North Atlantic TCs.

In this study, we leverage reanalysis-based estimates of TC outer size and the physics-based CLE15 wind model to reconstruct North Atlantic historical TC wind fields from 1950-2020 and model their associated storm tides using a high-resolution hydrodynamic model. We develop the first spatiotemporally continuous databases of R_{max} estimates for North Atlantic TCs from 1950-2020 and associated peak storm tides for the US Atlantic and Gulf coastline. Our database can supplement size estimates from IBTrACS or the Extended Best Track Database (EBTRK; Demuth et al. 2006) for storms occurring earlier than 1988 and can supplement previous storm tide databases (Marsooli and Lin, 2018; Muis et al., 2019) by similarly providing storm tide reconstructions for TCs occurring from 1950 onward. To evaluate our outer size and R_{max} estimates, we compare against two high-resolution TC wind field databases (QSCAT-R and HWIND) as well as against IBTrACS data. We evaluate the accuracy of our size estimates for the full TC life cycle of storms in both the low (equatorward of 30N) and middle (poleward of 30N) latitudes, and we investigate the uncertainty in the size estimates for storms undergoing extratropical transition (ET). Storm tide reconstructions are compared against observed peak water levels from tidal gauges along the US coastline. Finally, we demonstrate how our storm tide reconstructions impact storm surge hazard assessment at various US cities.

2. Methods

2.1. TC Datasets

North Atlantic TC track, intensity, and pressure information from 1950 onward are obtained from the IBTrACS Version 4 database (Knapp et al., 2010). To focus on TCs that can cause non-negligible storm surges, we select storms with maximum wind

144 speed greater than 17 m/s that approach within 200 km of the US coastline, resulting in
145 467 storms.
146 To estimate the outer TC wind field, we utilize the 0.25° latitude x 0.25°
147 longitude 3-h European Centre for Medium-range Weather Forecasts (ECMWF) ERA5
148 reanalysis dataset and back-extension (Hersbach et al., 2020). We choose the ERA5
149 reanalysis due to its relatively fine horizontal grid spacing compared to other reanalysis
150 datasets, its long temporal coverage (1950-2020), and because previous work (Bian et al.,
151 2020) demonstrated improved outer size representation of ERA5 compared to previous
152 reanalyses. We determine the position of each TC within the reanalysis grid by using the
153 IBTrACS position as a first guess. Then, using the sea-level pressure reanalysis fields we
154 calculate the centroid of pressure deficit and iteratively adjust the estimated TC center
155 position based on the method of Nguyen et al. (2014). Once given a center, we calculate
156 the azimuthal-mean wind field and calculate the radius of a given weak wind speed to
157 define storm size (details below).
158 Due to the lack of satellite data pre-1980 and data assimilation challenges in the
159 ERA5 back-extension (ECMWF, 2021), size and storm tide estimates from 1950-1979
160 have higher uncertainty compared to storms occurring from 1980 onward. Due to the
161 ERA5 back-extension data assimilation approach, some tropical cyclones from 1950-
162 1978 are represented with unrealistically intense Pmin values in the reanalysis data. We
163 do not utilize reanalysis-based Pmin estimates in our study, but the unphysical Pmin
164 values could impact the reanalysis representation of the outer TC wind field. Despite
165 larger uncertainties associated with size estimates for 1950-1979 TCs, a comparison of
166 the ERA5 size distributions pre- and post-1980 demonstrates that both groups of storms
167 have similar outer size climatologies (Figure S1) and similar R_{max} climatology (Figure
168 S2), suggesting that limitations within the 1950-1979 ERA5 data do not cause large
169 changes in the estimated TC sizes. As subsequent ERA5 1950-1978 versions are released,
170 our estimated size and storm surge estimates will be updated.
171 To validate reanalysis TC size estimates, we compare against IBTrACS and two
172 detailed TC wind field databases: the QuikSCAT Tropical Cyclone Radial Structure
173 database (QSCAT-R; Chavas and Vigh, 2014) and the HWind database (Powell et al.,
174 1998). Both QSCAT-R and HWind have been widely used to investigate features of the

inner (Chavas and Lin, 2016) and outer (Bian et al., 2021; Chavas et al., 2016; Schenkel et al., 2017) wind fields of historical TCs. QSCAT-R contains snapshots of azimuthal-mean 10-m azimuthal winds from 167 North Atlantic TCs between 2000-2009, and has a horizontal grid spacing of approximately 12.5 km. The HWind data used here comes from 120 North Atlantic TCs spanning 2004-2013 with approximate horizontal grid spacing of 6 km. QSCAT-R wind fields, which are based on NASA's QuikSCAT satellite (Chavas and Vigh, 2014), are available at irregular time points during each TC, while the HWind data is provided at 6-h intervals. QuikSCAT tends to underestimate wind speeds in high wind regimes (Stiles et al., 2014) and is therefore more suitable for investigating features of the outer TC wind field. We utilize the QSCAT-R dataset to validate the outer TC size estimates and use the higher resolution HWind dataset and IBTrACS data from 2004-2020 to validate the R_{max} estimates. Importantly, R_{max} estimates from IBTrACS are not reanalyzed post-storm and are based on near real-time information from aircraft reconnaissance or remotely-sensed data. Therefore, the IBTrACS R_{max} values may have significant uncertainty or errors. We utilize estimates of the IBTrACS R_{max} uncertainty that were developed by the National Hurricane Center (NHC) based on the 2021 North Atlantic and Northeast Pacific TC season (C. Landsea, personal communication, March 2022). The uncertainty estimates are based on mean absolute errors (MAEs) for the Best Track R_{max} values and are binned according to TC intensity (Table S1). The MAEs used here assume each storm is observed by both satellite and aircraft reconnaissance. Therefore, they represent conservative estimates of uncertainty as points far from land or without aircraft/satellite observations likely have much higher uncertainty. Moreover, as these estimates are derived from 2021 data, older storms in the IBTrACS dataset likely also have higher uncertainty. Nevertheless, the Best Track R_{max} errors described here provide a benchmark we can use to evaluate our model based R_{max} estimates.

2.2. TC Outer Size Estimation

Following Schenkel et al. (2017), we incorporate six outer size metrics defined as the radii at which the 10-m azimuthal-mean azimuthal wind speed equals 2, 4, 6, 8, 10, and 12 m/s (denoted $r_2 - r_{12}$). We consider a range of size metrics since not all wind radii may be defined at every point in time in the reanalysis data. To estimate each size metric

206 at each point in time, we follow Chavas and Vigh (2014). A TC-relative polar coordinate
207 is constructed and the reanalysis zonal and meridional winds are interpolated into the
208 polar grid, excluding all grid points over land. A uniform environmental wind is then
209 removed from the TC-relative zonal and meridional winds, which is estimated as 55% of
210 the translation speed and rotated 20 degrees counterclockwise according to Lin and
211 Chavas (2012). An asymmetry parameter (χ) is also calculated at each radius according
212 to Chavas and Vigh (2014). The χ parameter varies from 0 (perfect data symmetry about
213 the TC center) to 1 (complete asymmetry about the TC center) and quantifies the degree
214 of data coverage asymmetry at each radial distance. Radial bins with χ>0.5 are excluded
215 from the outer size estimation (Chavas and Vigh, 2014). The azimuthal-mean azimuthal
216 wind is then calculated, and followed by the extraction of outer size metrics (i.e. r_2, r_4, r_6,
217 r_8, r_{10}, r_{12}).
218 The reanalysis outer size estimates may be biased compared to the observations,
219 especially for the r_{10} and r_{12} metrics (Schenkel et al., 2017). Therefore, we bias correct
220 each outer size metric based on the comparison with the QSCAT-R outer sizes for the
221 period between 2000-2009. We find that the average outer size bias is generally constant
222 across the range of outer sizes for most size metrics (Figure S2), implying that the outer
223 size estimates can be corrected by simply adding a single correction value to each
224 estimate for a given metric. For each size metric (i.e. r_2 –r_{12}), the median difference
225 between the QSCAT-R values and the ERA5 estimates (shown as the horizontal red lines
226 in Figure 2a) are calculated and added to each ERA5 size estimate, similar to Bian et al.
227 (2021). Bias correction is applied to outer size estimates for all TCs from 1950 onward.
228
229 *2.3. Physics-based TC wind model and R_{max} estimation*
230 Several parametric TC wind models have been developed to represent the radial
231 profile of wind speed, and most models require free-fitting parameters as well as
232 estimates of V_{max} and R_{max} (Emanuel and Rotunno, 2011; Holland, 1980; Willoughby
233 et al., 2006). In contrast, the more recently developed CLE15 complete wind profile is a
234 fully physics-based model that describes the full TC wind field by merging solutions for
235 the inner convective region and the outer descending region. Wang et al. (2022) found
236 that the CLE15 model better reproduces observed TC wind fields compared to the

popularly used Holland model (Holland, 1980). As explained in Chavas and Lin (2016), the CLE15 wind profile can be constructed using V_{max} and a single additional outer wind radius. Chavas and Lin (2016) also demonstrated that CLE15 profiles based on V_{max} and outer size were able to reproduce the observed wind field variability of historical North Atlantic TCs. Therefore, we use the CLE15 model to construct the full wind profile and extract an estimate for R_{max} using the reanalysis-based outer size estimates and V_{max} from IBTrACS. More details about the CLE15 model formulation are documented in Chavas et al. (2015).

2.4 Time series of TC size estimates

A time series of R_{max} estimates are developed for each TC from 1950-2020 to match the IBTrACS time steps. For each 3-h increment, the TC outer size metrics (r_2-r_{12}) are estimated from the ERA5 reanalysis data, and bias corrected as explained above. Next, the maximum azimuthal-mean azimuthal wind (V^*_{max}) is calculated based on the IBTrACS V_{max} ($V_{max,BT}$) as follows:

$$V^*_{max} = 0.75(V_{max,BT} - 0.55V_{trans}) \quad (1)$$

where V_{trans} is the TC translation speed. We remove the background wind, estimated as 55% of the storm translation speed (Lin and Chavas, 2012), from $V_{max,BT}$ and then apply an additional 0.75 reduction factor similar to the reduction factor of 0.8 used in Chavas et al. (2016). This additional reduction factor takes into account that $V_{max,BT}$ represents the maximum wind speed occurring at any point in the TC, while we are interested in the maximum azimuthal-mean wind speed. The 0.75 reduction factor was developed by comparing the IBTrACS V_{max} estimates for all TCs from 2004-2013 with at least tropical storm intensity (>17 m/s) against the HWind maximum azimuthal-mean wind speeds (Figure S3).

Using each outer size estimate and V^*_{max}, we construct a radial profile of azimuthal-mean 10-m TC azimuthal winds using the CLE15 wind model and estimate R_{max}. If more than three outer size metrics are undefined for a particular time step, R_{max} is set as undefined. Since the CLE15 model may produce different R_{max} estimates using different outer size metrics, we create a weighted average R_{max} based on all defined outer size metrics with weights equal to the inverse of the root mean square error between the

reanalysis outer size estimates and the QSCAT-R outer size estimates (Table S2). Once the TC makes landfall, we do not utilize the reanalysis data to estimate outer size since our methodology sets reanalysis 10-m wind speeds over land are as undefined. Instead, we assume constant outer size after landfall equal to the last outer size estimate before landfall. Although TC size can change significantly after landfall (Chen and Chavas, 2020; Hlywiak and Nolan, 2021), our primary goal is to reconstruct TC storm surges, which would be minimally impacted by size changes occurring after landfall. The R_{max} at each point after landfall is estimated using V_{max}^{*} and constant outer size. Finally, we apply linear interpolation to fill in time steps where R_{max} is undefined due to insufficient outer size data, leading to a continuous time history of R_{max} values for each TC.

2.5 Defining Extratropical Transition (ET) Storms

Our study objectively defines extratropical transition (ET) using the cyclone phase space (Hart 2003; Evans and Hart 2003). ET start is defined when the TC transitions from a warm-core, nonfrontal cyclone to a warm-core, frontal cyclone. This occurs in the cyclone phase space when the storm-motion-relative 900–600-hPa layer thickness asymmetry across the TC exceeds an empirical value of 10 m. Positive thickness asymmetry parameter values correspond to cold and/or dry air to the left of motion and warm and/or moist air to the right of motion (Hart 2003; Evans and Hart 2003). ET end occurs when the TC transitions from a warm-core, frontal cyclone to a cold-core, frontal cyclone. This is defined as when the 900–600-hPa thermal wind changes from positive to negative. Negative values are associated with increases in the strength of the cyclone wind field with height (Hart 2003). Both cyclone phase space parameters are calculated over a 500-km radius from the TC center, which is the approximate length scale of North Atlantic TC outer size (Chavas et al. 2016; Schenkel et al 2018). We use ERA5 data available at intervals between 25-50 hPa to compute these parameters.

2.6 Estimating missing P_{min} data

For TCs occurring before 1975, P_{min} data is missing for some IBTrACS time steps. Although P_{min} is not a required input when estimating the storm R_{max}, P_{min} does

impact the modeled storm surge since the low-pressure TC center causes a small rise in ocean water level. The missing P_{min} data can be estimated using a simplification of the cyclostrophic balance equation (Knaff and Zehr, 2007):

$$P_{min} = P_{ref} - \left(\frac{V_{max}}{C}\right)^{1/n} \quad (2)$$

where C and n are empirically-derived coefficients that vary with latitude and were computed in Landsea et al. (2004), Table 7.5. Alternately, gradient wind balance can be used to relate the radial profiles of pressure and azimuthal wind speed, with the wind speed profile specified by the CLE15 model. Previous work by Chavas et al. (2017) showed that the application of the gradient wind balance theory can accurately predict the storm pressure deficit. A comparison of P_{min} estimated using the empirical cyclostrophic balance equation (2) and the gradient wind balance with CLE15 wind profile yielded similar results (Figure S4). Since calculating P_{min} using the gradient wind balance is more computationally expensive, we opt to use the simplified cyclostrophic balance equation in place of missing data.

2.7 Hydrodynamic modeling of TCs

To reconstruct storm tides from historical TCs, we couple the CLE15 wind model with the 2D, depth-integrated version of the advanced circulation (ADCIRC) hydrodynamic model (Luettich et al., 1992; Westerink et al., 1992). We utilize an unstructured computational mesh that spans the entire North Atlantic basin and has relatively high coastal resolution (~1 km). The mesh was developed and validated in Marsooli and Lin (2018). We also incorporate forcing from eight tidal constituents, which are estimated from the global model of ocean tides TPXO8-ATLAS (Egbert and Erofeeva, 2002). Recently, Wang et al. (2022) showed more accurate estimates of peak storm tides in ADCIRC when it was coupled to the CLE15 model compared to the Holland wind model. Based on the track, intensity and size time histories of each TC, ADCIRC simulates peak storm tides along the US Atlantic and Gulf coasts.

We compare our storm tide reconstructions to observed peak water levels from 74 NOAA tidal gauges (https://tidesandcurrents.noaa.gov) located along the US Atlantic and Gulf coasts. Observed water levels from all active tidal gauges within 200 km of each TC

329 track are compared against simulated storm tides. Gauges that were malfunctioning,
330 located within river or estuaries, or where water levels were clearly impacted by
331 freshwater discharges are excluded from the comparison. We divide the coastline into
332 five regions: western Gulf of Mexico (extending until New Orleans, LA), eastern Gulf of
333 Mexico, southeast Atlantic (until Chesapeake Bay), mid-Atlantic (until Connecticut), and
334 New England. Tidal gauges are grouped within each region to evaluate how well the
335 storm surge reconstructions match observations for different portions of the coast.
336

337 # 3. Results

338 *3.1 Representation of TC wind field within ERA5 reanalysis*

339 We first compare the radial structure of TC mean azimuthal wind from the ERA5
340 reanalysis and the QSCAT-R data. Figure 1 shows the median azimuthal-mean azimuthal
341 wind profile across all 6-h TC time steps between 2000-2009 with at least tropical storm
342 intensity from ERA5 and QSCAT-R. Although previous work found that ERA5 better
343 resolves TCs compared to the earlier ERA-Interim (Bian et al., 2021; Dullaart et al.,
344 2020), Fig. 1 shows that the reanalysis data still largely under resolves inner TC wind
345 speeds as expected from prior work (Schenkel et al. 2012; Schenkel et al. 2017). The
346 ERA5 data also overestimates R_{max} (Fig. 1) likely in part because of its coarse horizontal
347 resolution and conservative physics parameterizations (Schenkel et al. 2017; Bian et al.
348 2021). However, Fig. 1 also shows that ERA5 represents the outer TC wind field
349 accurately compared to QSCAT-R (Bian et al. 2021). For r>440 km, the median wind
350 profiles from the two datasets converge, and a Kolmogorov-Smirnov test at the 5% level
351 suggests that wind speeds from both datasets at each subsequent radii come from the
352 same distribution. The comparison of the wind profiles illustrates that ERA5 is a
353 reasonable source for estimating features of the outer wind field.

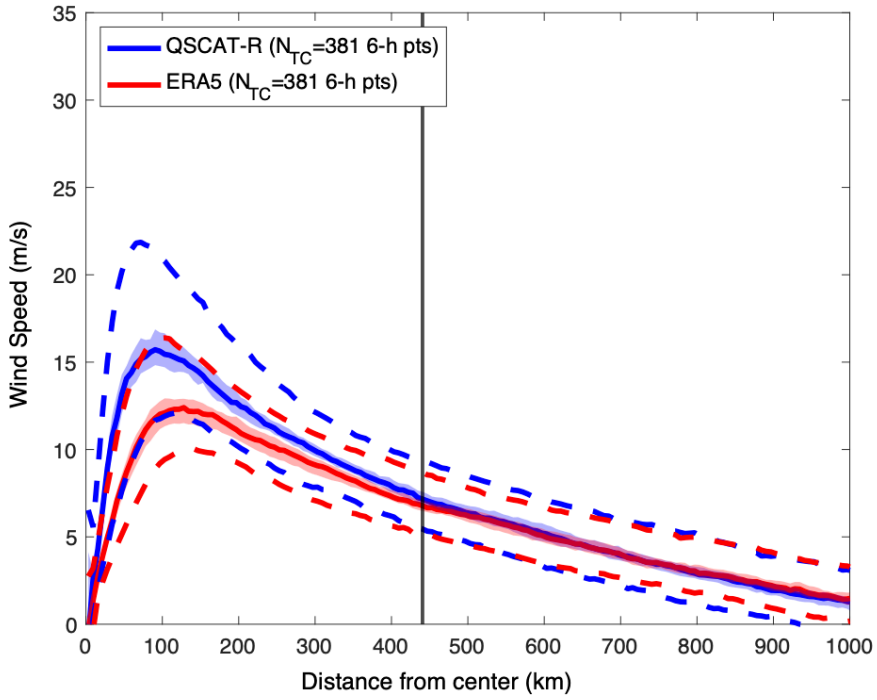

Figure 1: Median azimuthal wind profile (solid) with boot-strapped 95% confidence bounds (shaded) and inter-quartile range (IQR - dashed) for all QSCAT TC snapshots with Vmax greater than 17 m/s.

3.2 Accuracy of reanalysis-derived outer size metrics

After establishing that the TC outer wind profile from the ERA5 compares well to QSCAT-R, we next evaluate the accuracy of ERA5 outer size estimates. For each QSCAT-R data point and outer size metric (i.e. r_2, r_4, r_6, r_8, r_{10}, and r_{12}), we compare against the corresponding ERA5 sizes. The outer size analysis includes 381 QSCAT-R snapshots, although the size metrics are not all defined for each snapshot. Figure 2a shows boxplots of the difference between ERA5 and QSCAT-R for each size metric. Except for r_2, ERA5 slightly underestimates the outer size compared to QSCAT-R, with a larger negative bias for r_{10} and r_{12}. In contrast, the variability of the size estimates decreases for radii of higher wind speeds, demonstrated by the narrower interquartile ranges for r_{10} and r_{12}. The larger negative bias for r_{10} and r_{12} is due to ERA5 consistently under-predicting wind speeds for radial distances closer than 440 km (Fig. 1a) as found in previous studies (Bian et al., 2021; Schenkel et al., 2017).

Figure 2b shows a Taylor diagram (Taylor, 2001) comparing outer size in the ERA5 versus QSCAT-R. There is high correlation between ERA5 and QSCAT-R for all

size metrics, ranging from 0.8-0.93, with the highest correlations for r_{12} and r_8. The ratio of the standard deviations ranges from 0.8-1, indicating that there is less variability in the ERA5 sizes compared to QSCAT-R. The r_{12} and r_8 metrics have the lowest root-mean-square-error (RMSE), followed by r_6, r_{10}, r_4, and lastly r_2. As found in Schenkel et al. (2017), the lower correlation coefficient, higher RMSE, and higher normalized standard deviation for the r_2 metric suggests that the reanalysis data struggles to resolve weak azimuthal-mean TC wind speeds from the environmental background wind. Nevertheless, based on the relatively high correlation coefficients, low RMSE, and good match to QSCAT-R based outer sizes (Figure S3) for most other size metrics, the ERA5 reanalysis outer size estimates can be used (after bias correction) to realistically represent the outer TC wind field.

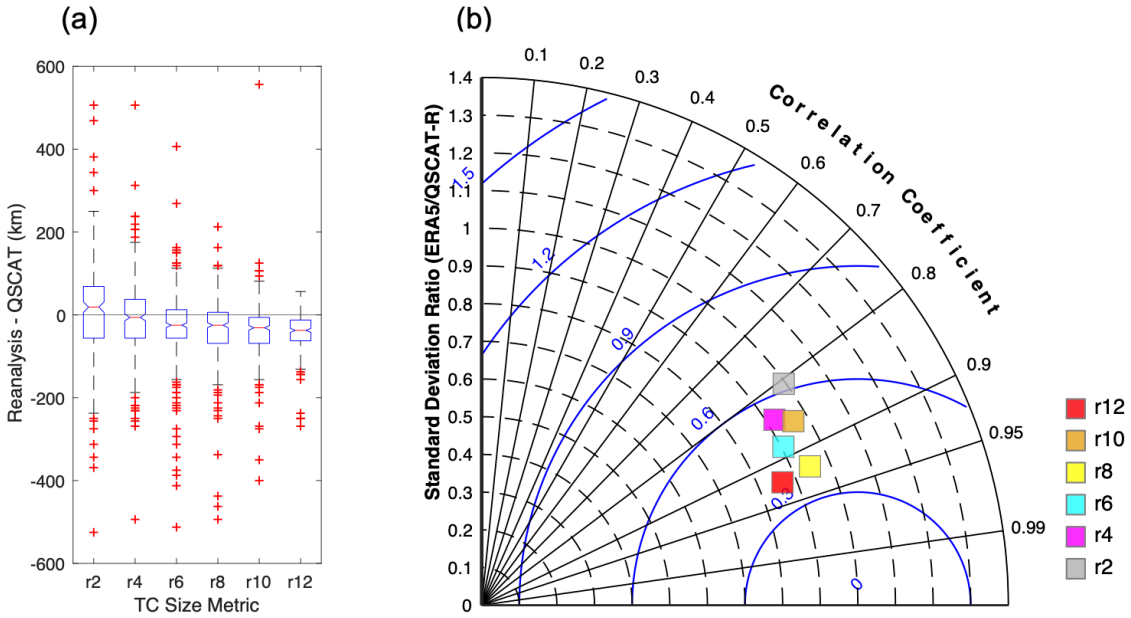

Figure 2: (a) Boxplots of outer size error of ERA5 reanalysis data compared to QSCAT-R for 381 TC snapshots at radii at which the azimuthal-mean 10-m azimuthal wind equals 12 m/s (r12), 10 m/s (r10), 8 m/s (r8), 6 m/s (r6), 4 m/s (r4) and 2 m/s (r2). Median of each metric shown as horizontal red line, and width of notch on each box denotes 95% uncertainty bounds of the median, calculated through bootstrapping. Red plus signs denote outliers using 1.5*IQR formula. (b) Pearson correlation (radial axis), ratio of standard deviations (y axis), and root mean square error (RMSE) between ERA5 and QSCAT (blue contours) for each outer size metric.

3.3 Accuracy of Rmax estimates

The ERA5 outer size estimates at each TC time step are bias corrected by adding the median difference between ERA5 and QSCAT-R outer size (red lines in Figure 2a)

calculated for each size metric (see Section 2.2). Then, using the bias corrected outer size estimates and V_{max}* defined in equation 1, we compute the azimuthal-mean 10-m wind field for each TC time step based on the CLE15 model and extract R_{max}. We compare the ERA5+CLE15 R_{max} values against R_{max} values from IBTrACS (Figure 3) and the high-resolution HWind dataset (Figure S5). Figure 3a shows a comparison of storm-averaged R_{max} for each TC between 2004-2020 for the duration of time when the TC is at least 100 km away from land and has intensity > 17.5 m/s. Figures 3b-e show a comparison of all 6-h time steps between 2004-2020 with intensity > 17.5 m/s and a distance to land of at least 100 km. Similarly, Figure S5 shows the same comparison for TC snapshots taken from HWind. The HWind R_{max} comparison illustrates that the model performs well overall: the RMSE is 31 km and the mean bias is only 0.3 km. Apart from a couple tropical storm intensity outliers, the vast majority of TC snapshots in Fig. S5 are clustered around the 1:1 line.

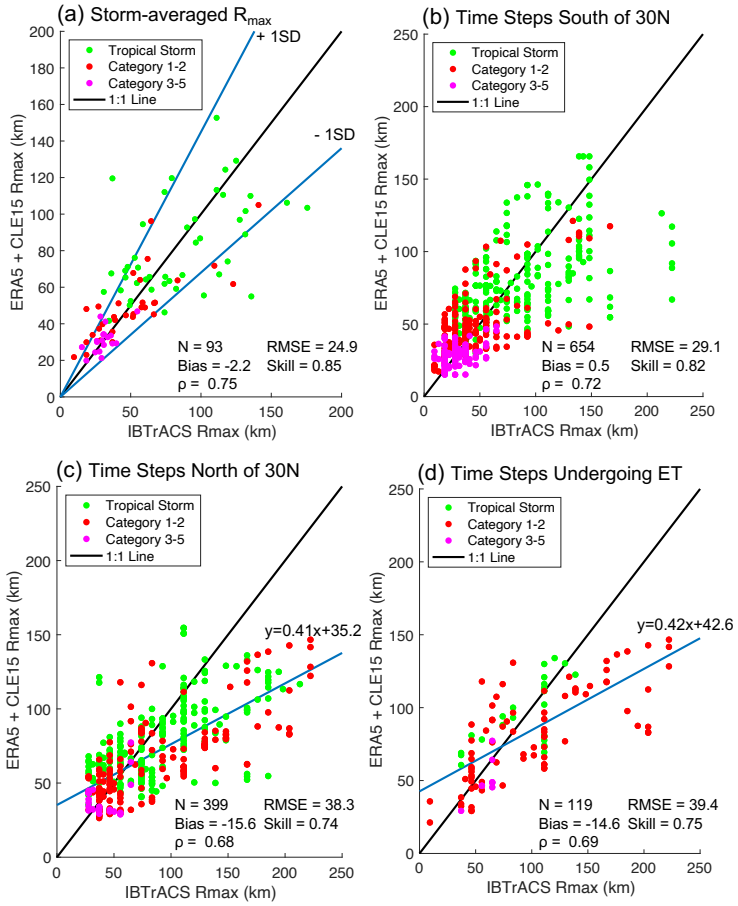

Figure 3: (a) Comparison between storm-averaged Rmax using ERA5 outer size and CLE15 wind profile (ERA5+CLE15) and IBTrACS Rmax for TCs where Vmax is greater than 17 m/s. Points

are colored by their Saffir-Simpson category. (b) Same as in (a) except using each 6-hour TC time step for TCs below 30 degrees latitude, (c) same as in b but for TC time steps above 30 degrees latitude, (d) same as in b but for extra-tropical transitioning (ET) time steps, where ET is defined according to the cyclone phase space (Hart, 2003).

3.3.1 Storm-Averaged Performance

Figure 3a shows a comparison between storm averaged R_{max} using ERA5+CLE15 and IBTrACS. R_{max} performance is quantified using three metrics: the RMSE, mean bias, and Willmott skill (Willmott, 1981), which quantifies the degree of agreement between modeled and observed data and ranges from 0 (complete disagreement) to 1 (complete agreement). The overall storm-averaged performance is relatively good, with a Willmott skill of 0.85 and average bias of -2.2 km. The variability in the difference between ERA5+CLE15 and IBTrACS increases with increasing R_{max}, suggesting that there is higher uncertainty for large R_{max} values. Additionally, the ERA5+CLE15 approach performs better in terms of storm averaged R_{max} for hurricane strength (>33 m/s) storms (red and magenta points) compared to tropical storm intensity (<33 m/s) events (green points), which tend to have larger R_{max} values. The lower ERA5+CLE15 performance for tropical storm intensity TCs could also be due to challenges extracting reanalysis outer size estimates from weak, less organized storms.

To measure the uncertainty associated with the ERA5+CLE15 R_{max} estimates, we develop a low and high estimate in addition to the modeled R_{max}. We first calculate the percent difference between the IBTrACS and ERA5+CLE15 storm averaged R_{max} values, which has a mean of approximately 0%. Then we scale all the R_{max} values up (down) by one standard deviation of the percent difference to get the high (low) estimate. Using this procedure, the low-high estimates overlap with the IBTrACS values for 68% of storms (close to +/- one standard deviation range of a normal distribution) shown in Fig. 3a.

3.3.2 Performance for Low-Latitude TCs

Fig. 3b shows the comparison between ERA5+CLE15 and IBTrACS R_{max} at each time step where a TC is below 30° N latitude. The ERA5+CLE15 approach performs well for low latitude TCs, with a mean bias of only 0.5 km and RMSE of 29.1 km. There are a few very large, weak TCs occurring below 30° N that are underestimated by ERA5+CLE15, and a few category 1-2 TC time steps that are also underestimated.

However, most TC time steps occurring below 30° N correlate well with the IBTrACS R_{max} and fall within the IBTrACS uncertainty bounds.

To further illustrate the performance of the modeled R_{max} values at low latitudes, Figure 4 shows the temporal evolution of R_{max} until landfall (where the plots terminate) based on ERA5+CLE15 (green) and IBTrACS R_{max} (blue) for three hurricanes that encompass a wide range of R_{max} evolution: (a) Katrina (2005), (b) Isaac (2012), and (c) Florence (2018). The model-based (+/- standard deviation) and IBTrACS (+/- MAE) R_{max} uncertainty ranges are also shown on each plot as shaded regions. For Isaac and Florence, the temporal evolution of modeled R_{max} tracks well with IBTrACS, as the ERA5+CLE15 approach is able to capture the shrinking/expanding TC size evolution. For Katrina's case, there is an increase in R_{max} occurring around hour 90 that is underestimated by ERA5+CLE15. Across all three storms the ERA5+CLE15 R_{max} values fall within the IBTrACS uncertainty bounds for the vast majority of time steps. Additionally, in most cases the IBTrACS values also fall within the ERA5+CLE15 uncertainty range. In the case of Isaac, the model initially overestimates R_{max}, but the ERA5+CLE15 and IBTrACS values converge as the storm intensifies. The examples shown in Figure 4 demonstrate that the ERA5+CLE15 R_{max} values can realistically reproduce TC size evolution for landfalling storms.

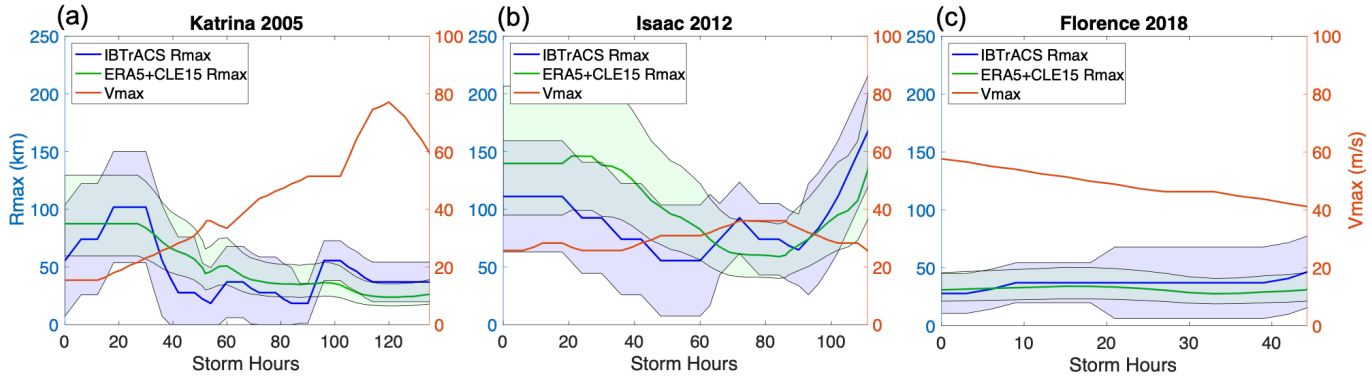

Figure 4: Evolution of IBTrACS Rmax (blue) and ERA5+CLE15 Rmax (green) with uncertainty bounds (shaded area), and Vmax (orange) for several major historical TCs occurring below 30N: (a) Katrina 2005, (b) Isaac 2012, (c) Florence 2018. ERA5+CLE15 uncertainty bounds are based on +/- one standard deviation (section 3c.1) and IBTrACS uncertainty bounds are based on +/- mean absolute error (MAE) as estimated by NHC.

3.3.3 Performance at Mid-Latitudes and for ET Storms

In contrast to the good performance at low latitudes, the performance of ERA5+CLE15 is not as good for mid-high latitude storms (Fig. 3c) where the model tends to underestimate Rmax for large storms, resulting in a mean bias of -15.6 km. The performance of ERA5 + CLE15 is also not as good for extratropical transitioning (ET) time steps (Fig. 3d), where ET time points are selected based on the cyclone phase space discussed in section 2.5. As shown in Figs. 3c and 3d, the majority of mid-latitude hurricane time steps (red points) whose sizes are underestimated by ERA5+CLE15 were also undergoing ET. Storm ET often results in an expansion and asymmetric evolution of the wind field (Evans and Hart, 2008; Hart and Evans, 2001; Jones et al., 2003), causing an increase in R_{max} (Evans et al., 2017; Evans and Hart, 2008; Halverson and Rabenhorst, 2013) that is demonstrated by the large R_{max} for category 1-2 storms shown in Fig. 3e. ET dynamics are not explicitly captured by the ERA5+CLE15 approach since the CLE15 wind profile is based on the angular momentum distribution of a mature TC. Still, ET wind field expansion could be partially accounted for in the ERA5+CLE15 R_{max} estimates: the ERA5-based outer size estimates may capture the expansion in the outer wind field during ET, and a larger outer size would yield a larger R_{max} using the CLE15 profile (for fixed intensity and latitude). Similarly, decreasing storm intensity and increasing latitude (both of which are also associated with ET) would yield increased R_{max} estimates from the CLE15 model.

Figure 5 shows the ERA5+CLE15 R_{max} (green) and IBTrACS R_{max} (blue) evolution for three TCs reaching the mid latitudes where ERA5+CLE15 does not perform as well: (a) Sandy (2012), (b) Jose (2017) and (c) Dorian (2019), where the vertical red line on each plot indicates ET start and the plot terminates either when the TC makes landfall or completes ET. In Sandy's case, the R_{max} had already begun expanding rapidly before ET started (according to the phase space criteria) as it transitioned from a TC into a warm-seclusion extratropical cyclone that had both tropical (warm core) and extra-tropical (frontal structure) features (Halverson and Rabenhorst, 2013). ERA5+CLE15 generally captures Sandy's R_{max} evolution until ET begins, at which point the IBTrACS R_{max} increases at a much faster rate than the model predicts, demonstrating that ERA5+CLE15 can capture some size expansion during ET but not completely. Similarly, during Dorian the modeled R_{max} expands once ET begins (Fig. 5c). However, the

IBTrACS R_{max} expanded at a faster rate during ET than was predicted by the model. Hurricane Jose (Fig. 5b) did not undergo ET according to the phase space criteria, but as the storm moved north it acquired some extra-tropical characteristics, which caused an increase in the storm's R_{max} (Berg, 2018).

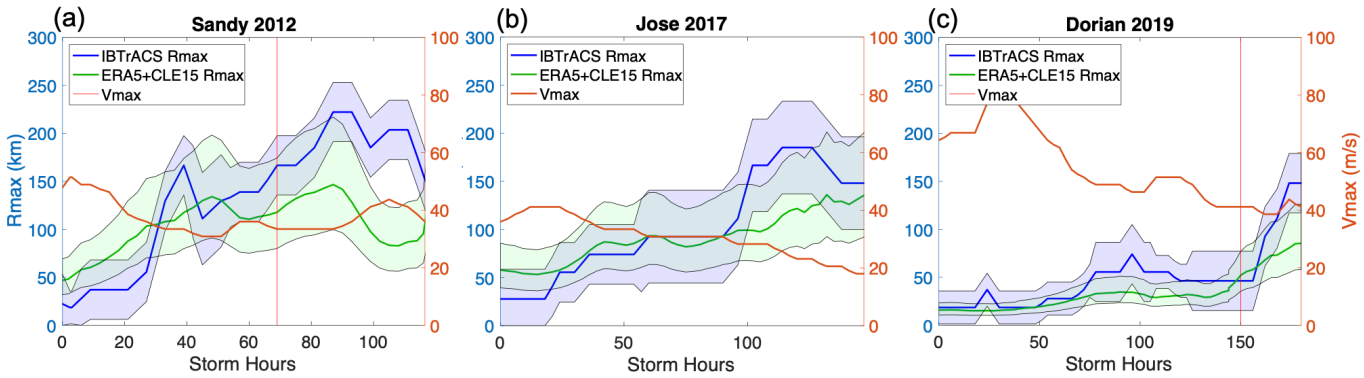

Figure 5: Evolution of IBTrACS Rmax (blue) and ERA5+CLE15 Rmax (green) with uncertainty bounds (shaded area), and Vmax (orange) for several major historical TCs reaching above 30 N: (a) Sandy (2012), (b) Jose (2017), and (c) Dorian (2019). ERA5+CLE15 uncertainty bounds are based on +/- one standard deviation (section 3c.1) and IBTrACS uncertainty bounds are based on +/- mean absolute error (MAE) as estimated by NHC. Vertical red line indicates time when extra-tropical transition (ET) begins according to the cyclone phase space and plots terminate when TC makes landfall or completes ET.

The ERA5+CLE15 R_{max} estimates for mid-latitude and ET storms cannot be corrected using a simple linear fit against the IBTrACS data. Figs 3c and 3e show that ERA5+CLE15 performs well for TC time steps where R_{max} is less than roughly 120 km (see small storms clustered around the 1:1 line) but tends to largely underestimate R_{max} for larger storms (see divergence from 1:1 line for large storms). For example, the mean bias for mid-latitude (ET) storms with R_{max} smaller than 120 km is only -2 km (-2.6 km), but is -60 km (-60 km) for mid-latitude (ET) storms larger than 120 km. However, the uncertainty associated with the IBTrACS R_{max} values may be larger for ET storms since the R_{max} is generally calculated as the location of highest wind speed occurring anywhere in the storm (compared to location of highest azimuthal-mean wind speed) and ET storms may have non-negligible asymmetry. Despite the larger negative bias and higher uncertainty for large ET storms, the ERA5+CLE15 approach produces reasonable TC size estimates that can be utilized for hazard analysis. Storm tides along the Mid-Atlantic and New England coastlines are less sensitive to R_{max} compared to other coastal regions (see section 3.4) and errors in R_{max} during ET do not result in large errors in peak storm

tide as shown in the next section (see Figure 6) Therefore, we use un-adjusted ERA5+CLE15 R_{max} estimates in conjunction with the low-high ranges developed in section 3.3.1.

3.4 Modeled and observed storm tides

In addition to developing a record of historical TC sizes, the second goal of our study is to develop a spatiotemporally continuous database of peak TC storm tides. We simulate peak storm tides using the ERA5+CLE15 size estimates and the ADCIRC hydrodynamic model (forced with the CLE15 wind model) and compare our modeled peak storm tides against peak water levels from 74 tidal gauges along the US coastline. Figure 6 shows scatterplots of observed and modeled peak storm tides, associated performance metrics, and error bars representing the low/high peak storm tides obtained from using the low/high R_{max} estimates at each active tidal gauge within each coastline region, where the regions are defined in Figure 8. Each point is colored based on the decade in which the storm occurred. Across all regions of the coastline, the reconstructed storm tides match well against observed peak water levels, with skill scores ranging from 0.89-0.97 and mean bias ranging from -0.12 – 0.03 m (where negative bias indicates model under prediction). Both the western and eastern Gulf of Mexico (GoM) have larger RMSE for peak storm tide estimates compared to locations along the Atlantic coast. The lower storm tide accuracy in the GoM is due to the coastline configuration and wide continental shelf, which causes storm tides to be highly sensitive to TC size in addition to TC intensity (Irish et al., 2008). Moreover, tidal amplitudes within the GoM are relatively small, so the wind-induced storm surge makes up a large component of the total water levels, while larger tidal ranges more strongly modulate total water levels along the Atlantic coast. Modeled storm tides along the GoM also tend to have larger uncertainty bars associated with a one standard deviation increase/decrease in Rmax, which also demonstrates that storm tides here are sensitive to TC size. Along the southeast and middle Atlantic, there is smaller error in the peak storm tide estimates, as demonstrated by the smaller RMSE values. The modeled and simulated storm tides match very closely in the New England region because the tidal amplitudes are large in this region and consequently the wind-induced surge makes up a smaller component of

the total water levels. Despite these differences in performance across different coastal regions, the comparisons shown in Figure 6 demonstrate that the models perform well for both early storms (1950-1979; see performance in Figure S7) and more recent storms (1980-2020).

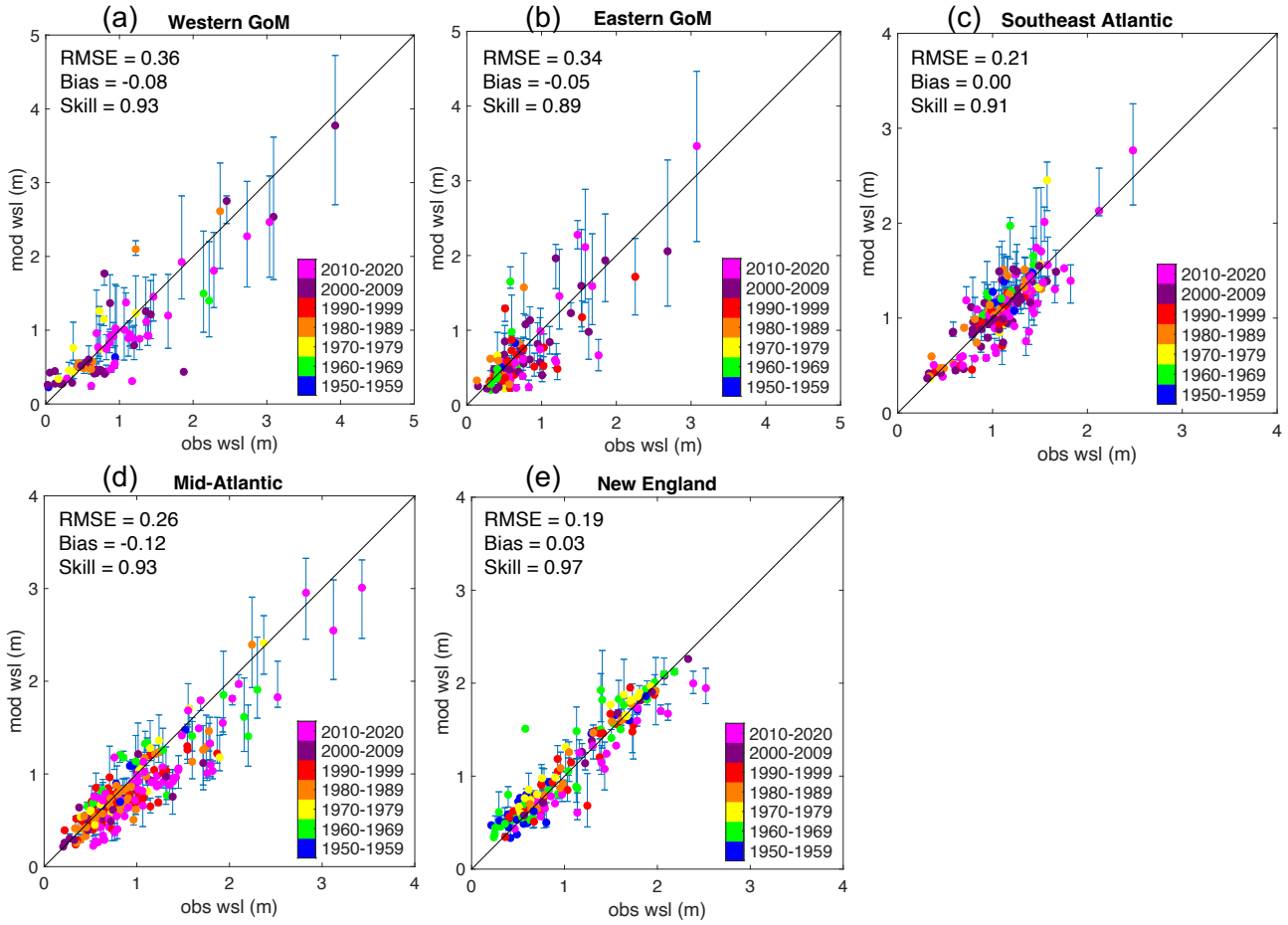

Figure 6: Comparison of modeled peak storm tides and observed peak storm tides for all historical TCs between 1950-2020 grouped into 5 regions: (a) Western Gulf of Mexico, (b) Eastern Gulf of Mexico, (c) Southeast Atlantic, (d) Mid-Atlantic, and (e) New England. Points are colored by decade and depict associated error bars (+/- one standard deviation of Rmax).

The errors between the observed and modeled storm tides could stem from multiple sources including uncertainty in R_{max}, TC position, or intensity from IBTrACS (Landsea and Franklin, 2013). Wave impacts, or errors stemming from the hydrodynamic mesh and/or physics of the ADCIRC model may also contribute to storm tide errors. Additionally, the parametric wind and pressure models used to represent the TC within ADCIRC may not match perfectly against the true TC wind/pressure fields. Therefore, to isolate the impact of the ERA5+CLE15 R_{max} estimate procedure, Figure 7 shows similar

comparisons of modeled and observed peak storm tides from 2004-2020, where red dots are modeled using ERA5+CLE15 estimated sizes and blue dots are based on the IBTrACS size. The difference in performance between ERA5+CLE15 storm tides and IBTrACS storm tides is small across all regions of the coastline, and the Willmott skill is slightly higher when using the ERA5+CLE15 R_{max} values in the eastern GoM and southeast Atlantic. For all regions the ERA5+CLE15 storm tides have a larger negative bias compared to the IBTrACS storm tides, but the high storm tide events are equally well captured by ERA5+CLE15. The mean bias for the mid-Atlantic is -0.16 m when using ERA5+CLE15 to estimate R_{max}, compared to -0.06 m when using the IBTrACS R_{max}. The slight underestimation of storm tides caused by using ERA5+CLE15 storm size estimates could be due to the CLE15 model's underestimation of R_{max} at mid-high latitudes and for ET storms (discussed in Section 3.3). Nevertheless, Fig. 7 shows that using ERA5+CLE15 to estimate the storm size does not result in significantly worse storm tide predictions compared to using the IBTrACS data. The storm tide performance metrics obtained by using the ERA5+CLE15 R_{max} estimates are also similar to the performance metrics reported in Marsooli et al. (2018), which utilized the same basin-scale mesh as this study and modeled storm tides for TCs from 1988-2015 using Extended Best Track (Demuth et al., 2006) R_{max}. Modeled peak storm tides from Marsooli et al. (2018) had an average RMSE, bias, and Willmott skill of 0.31, -0.04, and 0.90, respectively. In comparison, we report an average RMSE, bias, and Willmott skill of 0.29, -0.07, and 0.92 for all TCs from 2004-2020.

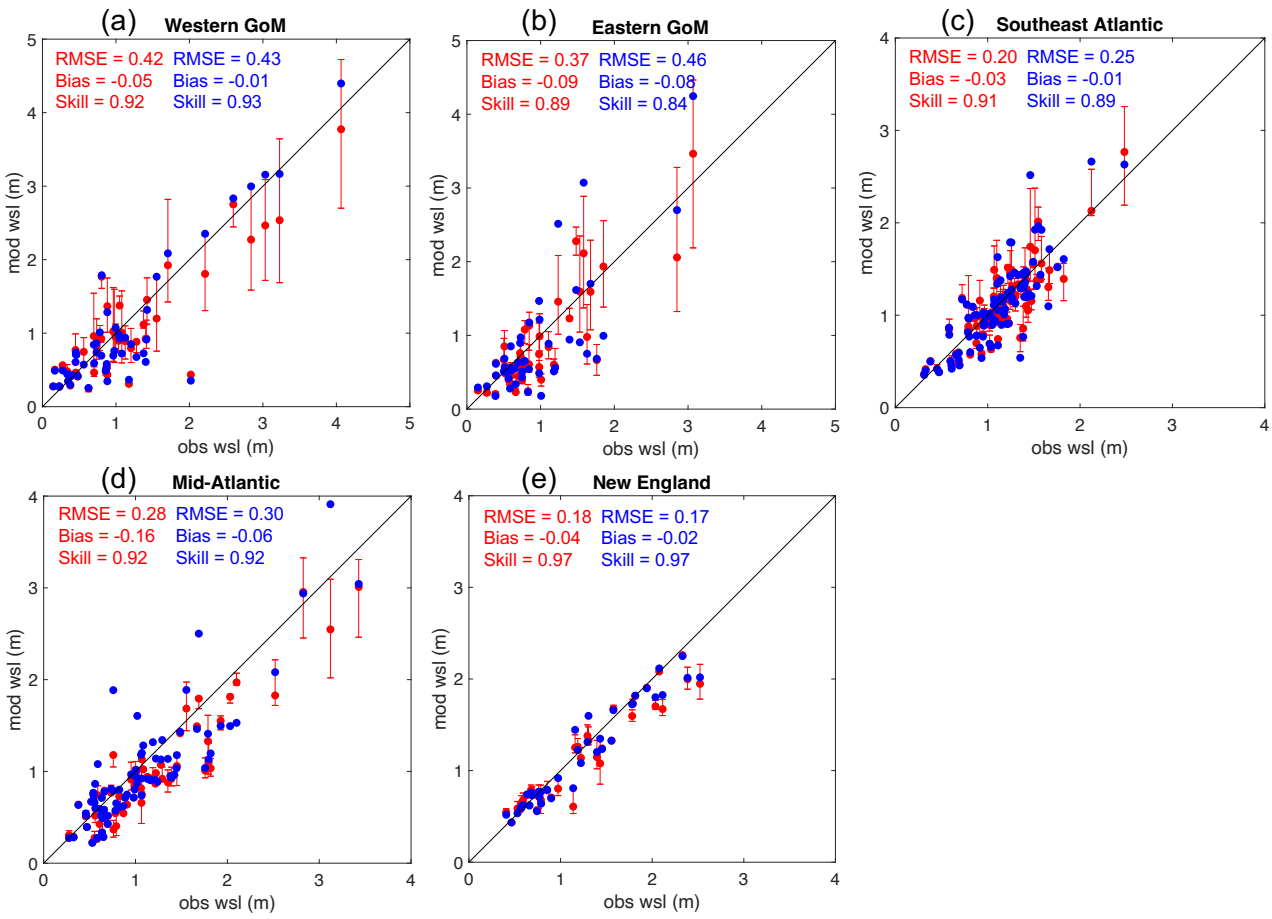

Figure 7: Comparison of modeled peak storm tides and observed peak storm tides for all historical TCs between 2004-2020 grouped into 5 regions: (a) Western Gulf of Mexico, (b) Eastern Gulf of Mexico, (c) Southeast Atlantic, (d) Mid-Atlantic, and (e) New England. Red points were modeled using ERA5+CLE15 TC size and blue points were modeled used IBTrACS size data.

3.5 Impact of TCs from 1950-1988 on storm surge hazard

To demonstrate the potential value of our reconstructions, we investigate how storm tides from TCs occurring between 1950-1987 can provide additional insight about coastal storm surge hazard. We model storm tides from 467 landfalling TCs, 227 of which occurred before 1988. Figure 8 shows which TCs caused the largest peak storm tides along different regions of the coastline. Along the mid-Atlantic and New England, Hurricane Sandy (2012) caused the highest storm tides for a large portion of the coastline. However, Hurricanes Hazel (1954) and Carol (1954) caused the most extreme storm surges in the Chesapeake Bay and Rhode Island, respectively. Hazel made landfall near the South/North Carolina boarder as a category 4 storm, and caused the highest storm tide levels along northern South Carolina and southern North Carolina, and in the

Chesapeake Bay. Hazel's intense winds prior to landfall funneled large amounts of water into the Chesapeake Bay and the resulting storm surge coincided with high tide, driving water levels even higher.

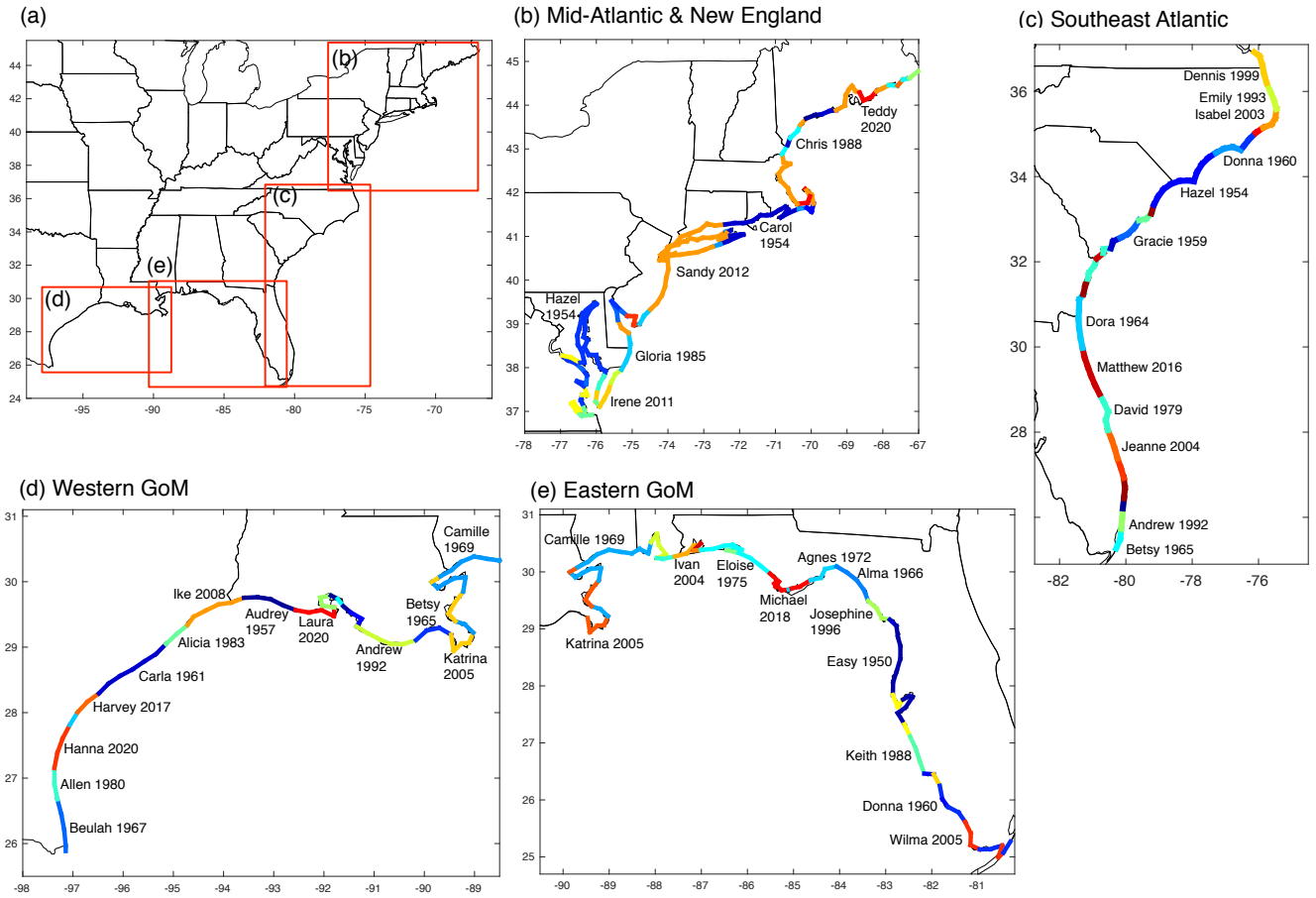

Figure 8: Storms that produced maximum modeled storm tides for different regions of the coastline (a): (b) Mid-Atlantic and New England, (c) Southeast Atlantic, (d) Western Gulf of Mexico, (e) Eastern Gulf of Mexico

In the southeast Atlantic (Fig. 8c) there are many storms before 1988 that caused the highest storm tides along different portions of the coast, including Hazel (1954), Gracie (1959), Dora (1964), and David (1979). Gracie made landfall nearly perpendicular to the coast as a category 4 storm along the southern South Carolina coast, causing widespread storm surge flooding despite arriving at low tide. In contrast, David moved parallel to the east coast of Florida as a weak hurricane, but still induced large storm tides in the Cape Canaveral region.

Similarly, along the eastern GoM (Fig. 8e) Camille (1969), Easy (1950) and Donna (1960) caused extreme storm surges. Camille, which made landfall near the border

635 of Louisiana and Mississippi, was the second most intense storm to strike the US, and
636 caused devastating storm tides that reached up to 6-9 m along the coastline of Mississippi
637 (ESSA, 1969; NBS, 1971). Along the western GoM, Beulah (1967) and Carla (1961)
638 were the most devastating pre-1988 TCs. Beulah was one of the most powerful
639 hurricanes to hit the lower Texas coast, causing widespread storm surges and coastal
640 erosion.

641 While Figure 8 illustrates which TCs caused the largest storm surge impacts, it
642 does not tell us how the incorporation of TCs from 1950-1987 impacts our estimates of
643 storm surge hazard. Incorporating a larger sample size of historical TCs occurring from
644 1950 to present can enable better estimation of storm surge return periods at different
645 coastal locations, especially at locations with a limited number of recent (post 1987) TC
646 occurrences. Figure 9 compares storm tide return period curves at several coastal
647 locations derived from modeled storm tides occurring from 1950-2020 (red) and similar
648 curves derived from only 1988-2020 TCs (blue). The curves in Fig. 9 were calculated by
649 fitting modeled storm tides with a generalized pareto distribution for the tail and
650 assuming TC arrivals occur as a Poisson process (Lin et al., 2012; Lin et al., 2010;
651 Marsooli et al., 2019). The shaded regions around each return period curve represent the
652 95% confidence intervals calculated according to the Delta method (Coles, 2001). The
653 locations in Figure 9 were chosen because there are significant differences between the
654 return period curves derived from the entire dataset compared to the more recent subset
655 of storms. At Port Isabel on the lower Texas coast, the extreme storm surges from Beulah
656 (1967) as well as Allen (1980) cause the 100-year storm tide estimate to increase from
657 0.97 m to 1.28 m above mean sea level. At Biloxi, MS, the extreme winds from Camille
658 (1969) caused 8 m of storm tide, which is over 3 m higher than the second highest storm
659 tide event (4.6 m caused by Katrina in 2005). The 100-year storm tide at Biloxi, MS
660 based on all storms from 1950-2020 is 4.6 m, while the 100-year estimate for 1988-2020
661 storms is only 3.7 m. Hurricane Camille is the primary data point causing an increase in
662 100-year storm tide: the incorporation of Camille's storm tide alone increases the 100-
663 year storm tide to 4.4 m.

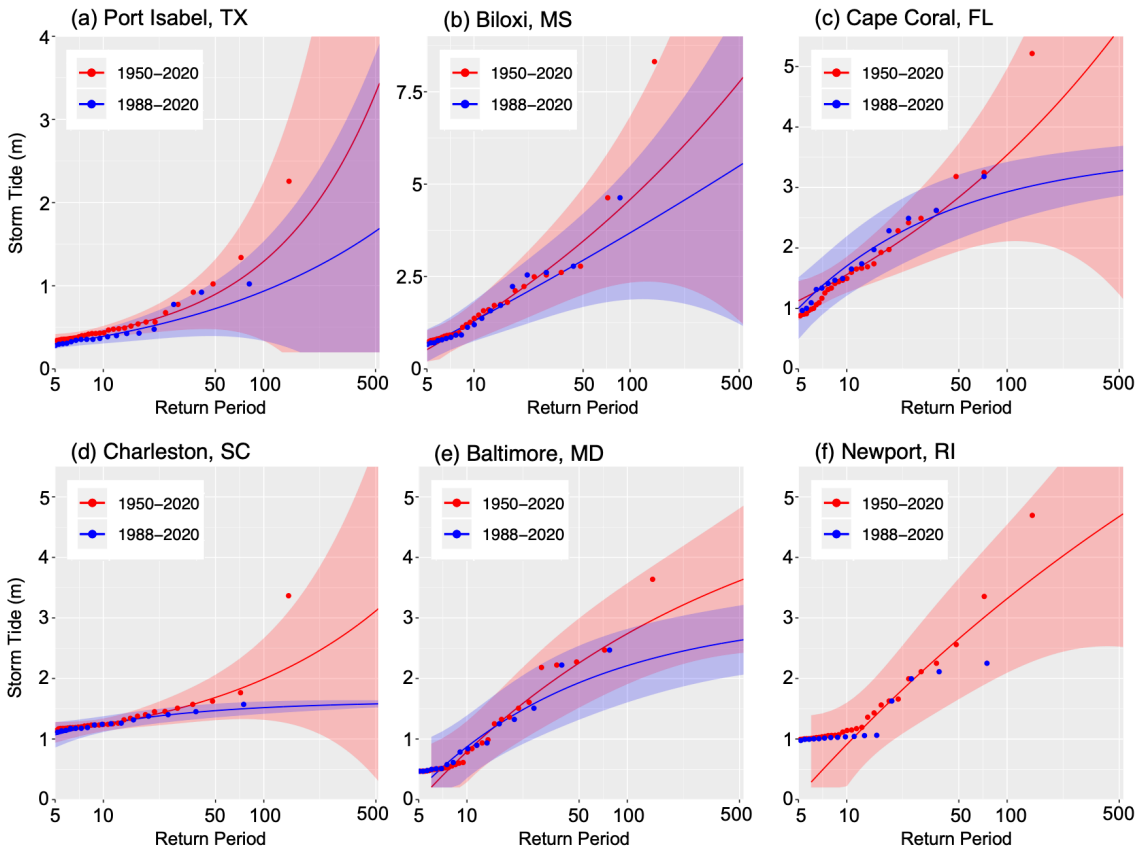

Figure 9: Storm tide return levels at select coastal locations using TCs from 1950-2020 (red) and using TCs from 1988-2020 (blue). Shading represents 95% confidence intervals and points represent individual storms.

Incorporating a larger sample size of events can also impact the estimated shape of the storm tide distribution at some locations. For example, at Cape Coral and Charleston incorporating storm tides from 1950-1987 changes the estimated tail behavior of the distribution from a bounded tail to an unbounded tail. Unbounded tail behavior causes the storm tide return level to increase exponentially with increasing log return period, albeit with higher uncertainty bounds as calculated through the Delta method. The return period estimates for a bounded versus unbounded distribution diverge increasingly for high storm tide values. For example, at Charleston the peak storm tide from Gracie (1959) was around 3.3 m, which is estimated as a 600-year event using the 1950-2020 return level curve. However, if we use the 1988-2020 curve, Gracie's return period would be undefined since the bounded tail distribution predicts zero probability for such a large event to occur. At Newport, RI the top three storm tide events all occurred before 1987

with the largest storm tide caused by hurricane Carol (1954). Because TC occurrences from 1988-2020 at Newport are so limited, it is not possible to fit a GP distribution to the 1988-2020 data. However, by incorporating the earlier TCs, it is possible to fit the GP distribution and obtain an estimate of the 100-year storm tide, which is 3.3 m.

The analysis presented here illustrates how the newly reconstructed storm tides from TCs occurring in 1950-1987 can provide valuable information about storm surge hazard across the US coastline. By developing continuous maps of peak storm tides, these reconstructions can supplement sparse gauge observations and provide a more complete understanding of historical TC storm surge hazard. Similarly, the reconstructed TC size data together with track and intensity data can be used to enhance estimates of historical TC wind (Wang et al., 2022) and rainfall, based on physical rainfall models (Feldmann et al., 2019; Xi et al., 2020; Zhu et al., 2013).

4 Discussion and Conclusions

In this study we develop a database of reconstructed historical TC sizes and storm tides based on a combination of reanalysis data and physics-based modeling. Specifically, we demonstrate that the ERA5 reanalysis data can represent TC outer size with good accuracy compared to observations. We then show that the physics-based CLE15 model can reasonably reproduce the TC R_{max} using Best Track intensity information and reanalysis-based outer size. Finally, we utilize the size reconstructions to develop a dataset of modeled coastal storm tides for TCs making landfall between 1950-2020 and demonstrate that the modeled storm tides compare well against tidal gauge observations.

The TC reconstruction methodology demonstrated here can be used in a variety of future applications, including quantification of wind, surge, and rainfall hazard, as well multi-hazard assessment (Gori et al., 2022; Moftakhari et al., 2017; Nasr et al., 2021; Song et al., 2020; Wahl et al., 2015). The TC size data generated here for the North Atlantic can also be combined with track and intensity data, and high-resolution ocean and atmosphere models to conduct detailed hindcast analysis of extreme winds, rainfall and storm surges (Lin et al., 2010) for pre-1988 TCs impacting the US coastline. The reconstructed size and storm tide data could also be used as input data for TC impact models (Hatzikyriakou et al., 2016; Nofal et al., 2021; Pilkington and Mahmoud,

712 2016) to reconstruct economic losses from historical TCs and conduct TC risk analysis.
713 The ERA5+CLE15 approach could also be applied to reconstruct sizes in other ocean
714 basins where TC data may be more limited or discontinuous (Knaff et al., 2018; Kossin et
715 al., 2013). The CLE15 model can be combined with climatological mean values of outer
716 size (Chavas et al., 2016; Chavas and Emanuel, 2010) to reconstruct TC wind fields and
717 storm surges for storms occurring before 1950, similar to the approach implemented in
718 Lin et al. (2014). Finally, the approach described here could be utilized with output from
719 general circulation models (GCMs) to evaluate changes in TC climatology and hazards
720 resulting from different climate warming scenarios.
721 The TC size and storm tide reconstructions developed here may be impacted by
722 limitations and uncertainties stemming from the ERA5 reanalysis data (discussed in
723 sections 2.2 and 3.2), CLE15 wind model (section 3.3), and hydrodynamic model and
724 mesh (section 3.4). Although there is higher uncertainty associated with the use of ERA5
725 to represent 1950-1979 TCs, storm tide modeling results suggest that our approach can
726 well-capture peak water levels induced by early TCs (Fig. S7). Similarly, despite some
727 underestimation of R_{max} for ET time steps (Fig. 3d), our modeling framework still
728 accurately simulates peak storm tides along the Mid-Atlantic and New England coastlines
729 (Fig 6d-e). Moreover, the ERA5+CLE15 approach performs with high skill and near-zero
730 bias for TC time steps below 30N (Fig 3b) and on a storm-averaged basis (Fig. 3a),
731 suggesting that our size reconstructions can reasonably represent pre-1988 TCs.
732
733 **Acknowledgements**
734 A.G. was supported by a National Defense Science & Engineering Graduate (NDSEG)
735 fellowship from the US Department of Defense. N.L. was supported by National Science
736 Foundation (NSF) grant number 1652448. D.C. was supported by NSF grant number
737 AGS 1945113.
738
739 **Data Availability Statement**
740 All data utilized in this study come from publicly available repositories (cited in the
741 manuscript). All data generated from this study, including estimated TC sizes and

742 modeled storm tides are deposited to the NSF DesignSafe-CI and can be freely assessed
743 online ([DOI to be provided upon acceptance]).
744
745 **References**

746 Bass, B., Irza, J.N., Proft, J., Bedient, P., Dawson, C., 2017. Fidelity of the integrated
747 kinetic energy factor as an indicator of storm surge impacts. Natural Hazards
748 85, 575–595. https://doi.org/10.1007/s11069-016-2587-3
749 Berg, R., 2018. National Hurricane Center Tropical Cyclone Report. Hurricane Jose.
750 Beven, J.L., Avila, L.A., Blake, E.S., Brown, D.P., Franklin, J.L., Knabb, R.D., Pasch, R.J.,
751 Rhome, J.R., Stewart, S.R., 2008. Atlantic hurricane season of 2005. Monthly
752 Weather Review 136, 1109–1173. https://doi.org/10.1175/2007MWR2074.1
753 Bian, G.F., Nie, G.Z., Qiu, X., 2021. How well is outer tropical cyclone size represented
754 in the ERA5 reanalysis dataset? Atmospheric Research 249, 105339.
755 https://doi.org/10.1016/j.atmosres.2020.105339
756 Blake, E., Kimberlain, T., Berg, R., Cangialosi, J., Beven II, J., 2013. Tropical Cyclone
757 Report: Hurricane Sandy.
758 Blake, E.S., Zelinsky, D.A., 2017. Tropical Cyclone Report: Hurricane Harvey.
759 Chavas, D.R., Emanuel, K.A., 2010. A QuikSCAT climatology of tropical cyclone size.
760 Geophysical Research Letters 37, 10–13.
761 https://doi.org/10.1029/2010GL044558
762 Chavas, D.R., Knaff, J.A., 2022. A simple model for predicting the hurricane radius of
763 maximum wind from outer size. Weather and Forecasting accepted, 1–20.
764 Chavas, D.R., Lin, N., 2016. A model for the complete radial structure of the tropical
765 cyclone wind field. Part II: Wind field variability. Journal of the Atmospheric
766 Sciences 73, 3093–3113. https://doi.org/10.1175/JAS-D-15-0185.1
767 Chavas, D.R., Lin, N., Dong, W., Lin, Y., 2016. Observed tropical cyclone size revisited.
768 Journal of Climate 29, 2923–2939. https://doi.org/10.1175/JCLI-D-15-0731.1
769 Chavas, D.R., Lin, N., Emanuel, K., 2015. A model for the complete radial structure of
770 the tropical cyclone wind field. Part I: Comparison with observed structure.
771 Journal of the Atmospheric Sciences 72, 3647–3662.
772 https://doi.org/10.1175/JAS-D-15-0014.1

773 Chavas, D.R., Reed, K.A., Knaff, J.A., 2017. Physical understanding of the tropical
774 cyclone wind-pressure relationship. Nature Communications 8.
775 https://doi.org/10.1038/s41467-017-01546-9
776 Chavas, D.R., Vigh, J., 2014. QSCAT-R: The QuikSCAT tropical cyclone radial structure
777 dataset. NCAR Tech. Note TN-513+STR.
778 Chen, J., Chavas, D.R., 2020. The Transient Responses of an Axisymmetric Tropical
779 Cyclone to Instantaneous Surface Roughening and Drying. Journal of the
780 Atmospheric Sciences 77, 2807–2834. https://doi.org/10.1175/JAS-D-19-
781 0320.1
782 Cline, I., 1900. Special Report on the Galveston Hurricane of September 8, 1900.
783 Coles, S., 2001. An Introduction to Statistical Modeling of Extreme Values. Springer-
784 Verlag, Bristol, UK.
785 Demuth, J.L., DeMaria, M., Knaff, J.A., 2006. Improvement of advanced microwave
786 sounding unit tropical cyclone intensity and size estimation algorithms. Journal
787 of Applied Meteorology and Climatology 45, 1573–1581.
788 https://doi.org/10.1175/JAM2429.1
789 Done, J.M., Ge, M., J. Holland, G., Dima-West, I., Phibbs, S., R. Saville, G., Wang, Y., 2020.
790 Modelling global tropical cyclone wind footprints. Natural Hazards and Earth
791 System Sciences 20, 567–580. https://doi.org/10.5194/nhess-20-567-2020
792 Dullaart, J.C.M., Muis, S., Bloemendaal, N., Aerts, J.C.J.H., 2020. Advancing global
793 storm surge modelling using the new ERA5 climate reanalysis. Climate
794 Dynamics 54, 1007–1021. https://doi.org/10.1007/s00382-019-05044-0
795 Dullaart, J.C.M., Muis, S., Bloemendaal, N., Chertova, M. V., Couasnon, A., Aerts, J.C.J.H.,
796 2021. Accounting for tropical cyclones more than doubles the global population
797 exposed to low-probability coastal flooding. Communications Earth &
798 Environment 2, 1–11. https://doi.org/10.1038/s43247-021-00204-9
799 ECMWF, 2021. ERA5 back extension 1950-1978 (Preliminary version): tropical
800 cyclones are too intense [WWW Document]. URL
801 https://confluence.ecmwf.int/display/CKB/ERA5+back+extension+1950-
802 1978+%28Preliminary+version%29%3A+tropical+cyclones+are+too+intense
803 (accessed 3.13.22).

804 Egbert, G.D., Erofeeva, S.Y., 2002. Efficient inverse modeling of barotropic ocean
805 tides. Journal of Atmospheric and Oceanic Technology 19, 183–204.
806 https://doi.org/10.1175/1520-0426(2002)019<0183:EIMOBO>2.0.CO;2
807 Emanuel, K., Rotunno, R., 2011. Self-stratification of tropical cyclone outflow. Part I:
808 Implications for storm structure. Journal of the Atmospheric Sciences 68, 2236–
809 2249. https://doi.org/10.1175/JAS-D-10-05024.1
810 ESSA, 1969. Hurricane Camille Preliminary Report.
811 Evans, C., Hart, R.E., 2008. Analysis of the wind field evolution associated with the
812 extratropical transition of Bonnie (1998). Monthly Weather Review 136, 2047–
813 2065. https://doi.org/10.1175/2007MWR2051.1
814 Evans, C., Wood, K.M., Aberson, S.D., Archambault, H.M., Milrad, S.M., Bosart, L.F.,
815 Corbosiero, K.L., Davis, C.A., Pinto, J.R.D., Doyle, J., Fogarty, C., Galarneau, T.J.,
816 Grams, C.M., Griffin, K.S., Gyakum, J., Hart, R.E., Kitabatake, N., Lentink, H.S.,
817 Mctaggart-Cowan, R., Perrie, W., Quinting, J.F.D., Reynolds, C.A., Riemer, M.,
818 Ritchie, E.A., Sun, Y., Zhang, F., 2017. The extratropical transition of tropical
819 cyclones. Part I: Cyclone evolution and direct impacts. Monthly Weather Review
820 145, 4317–4344. https://doi.org/10.1175/MWR-D-17-0027.1
821 Feldmann, M., Emanuel, K., Zhu, L., Lohmann, U., 2019. Estimation of atlantic tropical
822 cyclone rainfall frequency in the United States. Journal of Applied Meteorology
823 and Climatology 58, 1853–1866. https://doi.org/10.1175/JAMC-D-19-0011.1
824 Fritz, H.M., Blount, C., Sokoloski, R., Singleton, J., Fuggle, A., McAdoo, B.G., Moore, A.,
825 Grass, C., Tate, B., 2007. Hurricane Katrina storm surge distribution and field
826 observations on the Mississippi Barrier Islands. Estuarine, Coastal and Shelf
827 Science 74, 12–20. https://doi.org/10.1016/j.ecss.2007.03.015
828 Gori, A., Lin, N., Xi, D., Emanuel, K., 2022. Tropical cyclone climatology change greatly
829 exacerbates US extreme rainfall–surge hazard. Nature Climate Change 12, 171–
830 178. https://doi.org/10.1038/s41558-021-01272-7
831 Haigh, I.D., MacPherson, L.R., Mason, M.S., Wijeratne, E.M.S., Pattiaratchi, C.B.,
832 Crompton, R.P., George, S., 2014. Estimating present day extreme water level
833 exceedance probabilities around the coastline of Australia: Tropical cyclone-

induced storm surges. Climate Dynamics 42, 139–157. https://doi.org/10.1007/s00382-012-1653-0

Halverson, J.B., Rabenhorst, T., 2013. Hurricane Sandy: The Science and Impacts of a Superstorm. Weatherwise 66, 14–23. https://doi.org/10.1080/00431672.2013.762838

Hart, R.E., Evans, J.L., 2001. A climatology of the extratropical transition of Atlantic tropical cyclones. Journal of Climate 14, 546–564. https://doi.org/10.1175/1520-0442(2001)014<0546:ACOTET>2.0.CO;2

Hatzikyriakou, A., Lin, N., Gong, J., Xian, S., Hu, X., Kennedy, A., 2016. Component-Based Vulnerability Analysis for Residential Structures Subjected to Storm Surge Impact from Hurricane Sandy. Natural Hazards Review 17, 05015005. https://doi.org/10.1061/(asce)nh.1527-6996.0000205

Hersbach, H., Bell, B., Berrisford, P., Hirahara, S., Horányi, A., Muñoz-Sabater, J., Nicolas, J., Peubey, C., Radu, R., Schepers, D., Simmons, A., Soci, C., Abdalla, S., Abellan, X., Balsamo, G., Bechtold, P., Biavati, G., Bidlot, J., Bonavita, M., De Chiara, G., Dahlgren, P., Dee, D., Diamantakis, M., Dragani, R., Flemming, J., Forbes, R., Fuentes, M., Geer, A., Haimberger, L., Healy, S., Hogan, R.J., Hólm, E., Janisková, M., Keeley, S., Laloyaux, P., Lopez, P., Lupu, C., Radnoti, G., de Rosnay, P., Rozum, I., Vamborg, F., Villaume, S., Thépaut, J.N., 2020. The ERA5 global reanalysis. Quarterly Journal of the Royal Meteorological Society 146, 1999–2049. https://doi.org/10.1002/qj.3803

Hlywiak, J., Nolan, D.S., 2021. The Response of the Near-Surface Tropical Cyclone Wind Field to Inland Surface Roughness Length and Soil Moisture Content during and after Landfall. Journal of the Atmospheric Sciences 78, 983–1000. https://doi.org/10.1175/JAS-D-20-0211.1

Hodges, K., Cobb, A., Vidale, P.L., 2017. How well are tropical cyclones represented in reanalysis datasets? Journal of Climate 30, 5243–5264. https://doi.org/10.1175/JCLI-D-16-0557.1

Holland, G., 1980. An analytical model of wind and pressure profiles in hurricanes. Monthly Weather Review 108, 1212–1218.

Huffman, G.J., Pendergrass, A., NCAR, 2021. The Climate Data Guide: TRMM: Tropical Rainfall Measuring Mission [WWW Document].

Irish, J.L., Resio, D.T., Ratcliff, J.J., 2008. The influence of storm size on hurricane surge. Journal of Physical Oceanography 38, 2003–2013. https://doi.org/10.1175/2008JPO3727.1

Jones, S.C., Harr, P.A., Abraham, J., Bosart, L.F., Bowyer, P.J., Evans, J.L., Hanley, D.E., Hanstrum, B.N., Hart, R.E., Lalaurette, F., Sinclair, M.R., Smith, R.K., Thorncroft, C., 2003. The extratropical transition of tropical cyclones: Forecast challenges, current understanding, and future directions. Weather and Forecasting 18, 1052–1092. https://doi.org/10.1175/1520-0434(2003)018<1052:TETOTC>2.0.CO;2

Knabb, R.D., Rhome, J.R., Brown, D.P., 2005. Tropical Cyclone Report: Hurricane Katrina.

Knaff, J.A., Sampson, C.R., Musgrave, K.D., 2018. Statistical tropical cyclone wind radii prediction using climatology and persistence: Updates for the western North Pacific. Weather and Forecasting 33, 1093–1098. https://doi.org/10.1175/WAF-D-18-0027.1

Knaff, J.A., Zehr, R.M., 2007. Reexamination of tropical cyclone wind-pressure relationships. Weather and Forecasting 22, 71–88. https://doi.org/10.1175/WAF965.1

Knapp, K.R., Kruk, M.C., Levinson, D.H., Diamond, H.J., Neumann, C.J., 2010. The international best track archive for climate stewardship (IBTrACS). Bull Am Meteorol Soc 91, 363–376. https://doi.org/10.1175/2009BAMS2755.1

Kossin, J.P., Olander, T.L., Knapp, K.R., 2013. Trend analysis with a new global record of tropical cyclone intensity. Journal of Climate 26, 9960–9976. https://doi.org/10.1175/JCLI-D-13-00262.1

Landsea, C.W., Anderson, C., Charles, N., Clark, G., Dunion, J., Fernandez-Partagas, J., Hungerford, P., Neumann, C., Zimmer, M., 2004. The Atlantic hurricane database re-analysis project: Documentation for the 1851-1910 alterations and additions to the HURDAT database. Hurricanes and Typhoons: Past, Present, and Future 177–221.

895 Landsea, C.W., Franklin, J.L., 2013. Atlantic hurricane database uncertainty and
896 presentation of a new database format. Monthly Weather Review 141, 3576–
897 3592. https://doi.org/10.1175/MWR-D-12-00254.1
898 Lin, N., Chavas, D., 2012. On hurricane parametric wind and applications in storm
899 surge modeling. Journal of Geophysical Research Atmospheres 117, 1–19.
900 https://doi.org/10.1029/2011JD017126
901 Lin, N., Emanuel, K., Oppenheimer, M., Vanmarcke, E., 2012. Physically based
902 assessment of hurricane surge threat under climate change. Nature Climate
903 Change 2, 462–467. https://doi.org/10.1038/nclimate1389
904 Lin, N., Emanuel, K.A., Smith, J.A., Vanmarcke, E., 2010. Risk assessment of hurricane
905 storm surge for New York City. Journal of Geophysical Research Atmospheres
906 115, 1–11. https://doi.org/10.1029/2009JD013630
907 Lin, N., Lane, P., Emanuel, K.A., Sullivan, R.M., Donnelly, J.P., 2014. Heightened
908 hurricane surge risk in northwest Florida revealed from climatological-
909 hydrodynamic modeling and paleorecord reconstruction. Journal of
910 Geophysical Research 119, 8606–8623.
911 https://doi.org/10.1002/2014JD021584
912 Lin, Ning, Smith, J.A., Villarini, G., Marchok, T.P., Baeck, M.L., 2010. Modeling Extreme
913 Rainfall, Winds, and Surge from Hurricane Isabel (2003). Weather and
914 Forecasting 25, 1342–1361. https://doi.org/10.1175/2010waf2222349.1
915 Lin, Y., Mitchell, K.E., 2005. The NCEP Stage II/IV hourly precipitation analyses:
916 Development and applications, in: 19th Conf. on Hydrology. Amer. Meteor. Soc.,
917 San Diego, CA.
918 Liu, M., Vecchi, G.A., Smith, J.A., Knutson, T.R., 2019. Causes of large projected
919 increases in hurricane precipitation rates with global warming. npj Climate and
920 Atmospheric Science 2, 1–5. https://doi.org/10.1038/s41612-019-0095-3
921 Luettich, R.A., Westerink, J.J., Scheffner, N.W., 1992. ADCIRC: An advanced three-
922 dimensional circulation model for shelves, coasts, and estuaries. Report 1:
923 Theory and methodology of ADCIRC-2DDI and ADCIRC-3DL. Vicksburg, Miss.
924 Marsooli, R., Lin, N., 2018. Numerical Modeling of Historical Storm Tides and Waves
925 and Their Interactions Along the U.S. East and Gulf Coasts. Journal of

926 Geophysical Research: Oceans 3844–3874.
927 https://doi.org/10.1029/2017JC013434
928 Marsooli, R., Lin, N., Emanuel, K., Feng, K., 2019. Climate change exacerbates
929 hurricane flood hazards along US Atlantic and Gulf Coasts in spatially varying
930 patterns. Nature Communications 10, 1–9. https://doi.org/10.1038/s41467-
931 019-11755-z
932 Menne, M.J., Durre, I., Vose, R.S., Gleason, B.E., Houston, T.G., 2012. An overview of
933 the global historical climatology network-daily database. Journal of
934 Atmospheric and Oceanic Technology 29, 897–910.
935 https://doi.org/10.1175/JTECH-D-11-00103.1
936 Merrill, R., 1984. A Comparison of Large and Small Tropical Cyclones. Monthly
937 Weather Review 112, 1408–1418.
938 Moftakhari, H.R., Salvadori, G., AghaKouchak, A., Sanders, B.F., Matthew, R.A., 2017.
939 Compounding effects of sea level rise and fluvial flooding. Proceedings of the
940 National Academy of Sciences 114, 9785–9790.
941 https://doi.org/10.1073/pnas.1620325114
942 Muis, S., Lin, N., Verlaan, M., Winsemius, H.C., Ward, P.J., Aerts, J.C.J.H., 2019.
943 Spatiotemporal patterns of extreme sea levels along the western North-Atlantic
944 coasts. Scientific Reports 9, 1–12. https://doi.org/10.1038/s41598-019-40157-
945 w
946 Nasr, A.A., Wahl, T., Rashid, M.M., Camus, P., Haigh, I.D., 2021. Assessing the
947 dependence structure between oceanographic, fluvial, and pluvial flooding
948 drivers along the United States coastline. Hydrology and Earth System Sciences
949 25, 6203–6222. https://doi.org/10.5194/hess-25-6203-2021
950 NBS, 1971. NBS Technical Note 569: Hurricane Camille - August 1969. Washington,
951 D. C.
952 Needham, H.F., Keim, B.D., 2012. A storm surge database for the US Gulf Coast.
953 International Journal of Climatology 32, 2108–2123.
954 https://doi.org/10.1002/joc.2425

955 Needham, H.F., Keim, B.D., Sathiaraj, D., 2015. A review of tropical cyclone-generated
956 storm surges: Global data sources, observations, and impacts. Reviews of
957 Geophysics 53, 545–591. https://doi.org/10.1002/2014RG000477
958 Nguyen, L.T., Molinari, J., Thomas, D., 2014. Evaluation of tropical cyclone center
959 identification methods in numerical models. Monthly Weather Review 142,
960 4326–4339. https://doi.org/10.1175/MWR-D-14-00044.1
961 Nofal, O.M., van de Lindt, J.W., Do, T.Q., Yan, G., Hamideh, S., Cox, D.T., Dietrich, J.C.,
962 2021. Methodology for Regional Multihazard Hurricane Damage and Risk
963 Assessment. Journal of Structural Engineering 147, 04021185.
964 https://doi.org/10.1061/(asce)st.1943-541x.0003144
965 Pilkington, S.F., Mahmoud, H.N., 2016. Using artificial neural networks to forecast
966 economic impact of multi-hazard hurricane-based events. Sustainable and
967 Resilient Infrastructure 1, 63–83.
968 https://doi.org/10.1080/23789689.2016.1179529
969 Powell, M.D., Houston, S.H., Amat, L.R., Morisseau-Leroy, N., 1998. The HRD real-time
970 hurricane wind analysis system. Journal of Wind Engineering and Industrial
971 Aerodynamics 77–78, 53–64. https://doi.org/10.1016/S0167-6105(98)00131-
972 7
973 Pugh, D., 1987. Tides, Surges and Mean Sea-Level. John Wiley & Sons, Chichester.
974 Ramos-Valle, A.N., Curchitser, E.N., Bruyère, C.L., 2020. Impact of Tropical Cyclone
975 Landfall Angle on Storm Surge Along the Mid-Atlantic Bight. Journal of
976 Geophysical Research: Atmospheres 125, 1–19.
977 https://doi.org/10.1029/2019JD031796
978 Schenkel, B.A., Hart, R.E., 2012. An examination of tropical cyclone position,
979 intensity, and intensity life cycle within atmospheric reanalysis datasets.
980 Journal of Climate 25, 3453–3475. https://doi.org/10.1175/2011JCLI4208.1
981 Schenkel, B.A., Lin, N., Chavas, D., Oppenheimer, M., Brammer, A., 2017. Evaluating
982 outer tropical cyclone size in reanalysis datasets using QuikSCAT data. Journal
983 of Climate 30, 8745–8762. https://doi.org/10.1175/JCLI-D-17-0122.1
984 Schenkel, B.A., Lin, N., Chavas, D., Vecchi, G.A., Oppenheimer, M., Brammer, A., 2018.
985 Lifetime evolution of outer tropical cyclone size and structure as diagnosed

from reanalysis and climate model data. Journal of Climate 31, 7985–8004. https://doi.org/10.1175/JCLI-D-17-0630.1

Smith, A.B., Katz, R.W., 2013. US billion-dollar weather and climate disasters: Data sources, trends, accuracy and biases. Natural Hazards 67, 387–410. https://doi.org/10.1007/s11069-013-0566-5

Song, J.Y., Alipour, A., Moftakhari, H.R., Moradkhani, H., 2020. Toward a more effective hurricane hazard communication. Environmental Research Letters 15. https://doi.org/10.1088/1748-9326/ab875f

Stiles, B.W., Danielson, R.E., Poulsen, W.L., Brennan, M.J., Hristova-Veleva, S., Shen, T.P., Fore, A.G., 2014. Optimized tropical cyclone winds from quikscat: A neural network approach. IEEE Transactions on Geoscience and Remote Sensing 52, 7418–7434. https://doi.org/10.1109/TGRS.2014.2312333

Taylor, K.E., 2001. Summarizing multiple aspects of model performance in a single diagram. Journal of Geophysical Research 106, 7183–7192.

Thomas, A., Dietrich, J.C., Asher, T.G., Bell, M., Blanton, B.O., Copeland, J.H., Cox, A.T., Dawson, C.N., Fleming, J.G., Luettich, R.A., 2019. Influence of storm timing and forward speed on tides and storm surge during Hurricane Matthew. Ocean Modelling 137, 1–19. https://doi.org/10.1016/j.ocemod.2019.03.004

Wahl, T., Jain, S., Bender, J., Meyers, S.D., Luther, M.E., 2015. Increasing risk of compound flooding from storm surge and rainfall for major US cities. Nature Climate Change 1–6. https://doi.org/10.1038/NCLIMATE2736

Westerink, J.J., Luettich, R.A., Blain, C.A., Scheffner, N.W., 1992. ADCIRC: An advanced three-dimensional circulation model for shelves, coasts, and estuaries. Report 2: User's Manual for ADCIRC-2DDI. Vicks- burg, Miss.

Willmott, C.J., 1981. On the validation of models. Physical Geography 2, 184–194. https://doi.org/10.1080/02723646.1981.10642213

Willoughby, H.E., Darling, R.W.R., Rahn, M.E., 2006. Parametric representation of the primary hurricane vortex. Part II: A new family of sectionally continuous profiles. Monthly Weather Review 134, 1102–1120. https://doi.org/10.1175/MWR3106.1

Woodruff, J.D., Irish, J.L., Camargo, S.J., 2013. Coastal flooding by tropical cyclones and sea-level rise. Nature 504, 44–52. https://doi.org/10.1038/nature12855

Xi, D., Lin, N., Smith, J., 2020. Evaluation of a physics-based tropical cyclone rainfall model for risk assessment. Journal of Hydrometeorology 21, 2197–2218. https://doi.org/10.1175/JHM-D-20-0035.1

Zhang, W., Villarini, G., Vecchi, G.A., Smith, J.A., 2018. Urbanization exacerbated the rainfall and flooding caused by hurricane Harvey in Houston. Nature 563, 384–388. https://doi.org/10.1038/s41586-018-0676-z

Zhu, L., Quiring, S.M., Emanuel, K.A., 2013. Estimating tropical cyclone precipitation risk in Texas. Geophysical Research Letters 40, 6225–6230. https://doi.org/10.1002/2013GL058284